Journal of the European Ceramic Society 46 (2026) 117777

Contents lists available at ScienceDirect

Journal of the European Ceramic Society

journal homepage: www.elsevier.com/locate/jeurceramsoc

3D printed glass-based biophotonic scaffolds for in situ activation of photoswitchable drugs

Evellyn Santos Magalhães [a,*], Nirajan Ojha [a], Sonya Ghanavati [b], Ekin Opar [c,h], Philippe F. Smet [d], Mika Lastusaari [e], Fabio Riefolo [c,1], Carlo Matera [c,2], Jonathan Massera [b,*], Pau Gorostiza [c,f,g,**], Laeticia Petit [a,*]

[a] Photonics Laboratory, Tampere University, Korkeakoulunkatu 3, Tampere 33720, Finland
[b] Faculty of Medicine and Health Technology, Tampere University, Korkeakoulunkatu 3, Tampere 33720, Finland
[c] Institute for Bioengineering of Catalonia (IBEC), The Barcelona Institute for Science and Technology (BIST), Carrer de Baldiri Reixac 10, Barcelona 08028, Spain
[d] LumiLab, Department of Solid State Sciences, Ghent University, Krijgslaan 281-S1, Gent 9000, Belgium
[e] Department of Chemistry, University of Turku, Turku FI-20014, Finland
[f] Catalan Institution for Research and Advanced Studies (ICREA), Barcelona 08010, Spain
[g] Network Research Center on Bioengineering, Biomaterials, and Nanomedicine, Barcelona 08028, Spain
[h] Doctorate Program in Engineering and Applied Science, Universitat de Barcelona, Barcelona, Spain

ARTICLE INFO

Keywords:
Bioactive glass
Scaffold
$CaWO_4$ upconverter crystals
Persistent luminescence
Photoswitchable molecule

ABSTRACT

The fabrication of porous biophotonic scaffold using a robocasting is reported here. Such material could be used for in-situ activation of photoswitchable drugs, which is essential for improving therapeutic efficacy while minimizing side effects. The scaffold is made of a phosphate glass mixed with $CaWO_4$:Yb^{3+},Tm^{3+} crystals and $SrAl_2O_4$:Eu^{2+},Dy^{3+} phosphors. Upon 980 nm irradiation, the scaffold emits blue light and green afterglow, enabling in-situ activation post-implantation as NIR light penetrates tissue. The challenges related to the sintering process and its effect on the spectroscopic properties of the scaffold are discussed. The as-3D printed scaffold successfully enables one to activate the muscarinic photoswitchable drug Phthal Azobenzene Iperoxo (PAI) upon NIR excitation, confirming the potential for in-situ phototriggered delivery of drug action using tissue-permeable light stimulus.

1. Introduction

Bioactive glasses have been extensively used in tissue engineering for the regeneration, repair, and replacement of damaged tissues. This is due to their ability to release therapeutic ions and to form an apatite layer when dissolved in physiological fluids [1]. They are highly versatile and have been utilized in various forms, including coatings, particles, bone cements, and scaffolds, making them suitable for a wide range of tissue regeneration and repair applications. [2]. The most commercially used bioactive glasses in clinical settings are 45S5 [3] and S53P4 [4], both being silicate glasses. Phosphate glasses have been also materials of interest as bioactive glasses as they can be engineered to exhibit higher solubility and ion release compared to silica-based glasses [5]. Phosphate bioactive glasses are unique materials with fully resorbable characteristics, making them favorable for hard and soft tissue engineering [6–8]. The composition of phosphate glass can be readily tailored to achieve controlled ion release, congruent dissolution, and enhanced resistance to crystallization properties. Recently, Ghanavati et al. demonstrated the successful preparation of 3D porous scaffolds from the phosphate glass with the composition 45 P_2O_5 – 20CaO - 10MgO – 10SrO – 10Na_2O – 2.5B_2O_3 – 2.5SiO_2 (in mol%) [8].

Such scaffolds have been of great interest in medical treatments as

* Corresponding authors.
** Corresponding author at: Institute for Bioengineering of Catalonia (IBEC), The Barcelona Institute for Science and Technology (BIST), Carrer de Baldiri Reixac 10, Barcelona 08028, Spain.
E-mail addresses: evellyn.santosmagalhaes@tuni.fi (E.S. Magalhães), jonathan.massera@tuni.fi (J. Massera), pau@icrea.cat (P. Gorostiza), laeticia.petit@tuni.fi (L. Petit).
[1] Present address: Teamit Institute, Partnerships, Barcelona Health Hub, 08025 Barcelona, Spain
[2] Present address: Department of Pharmaceutical Sciences, University of Milan, Via L. Mangiagalli 25, 20133 Milan, Italy

https://doi.org/10.1016/j.jeurceramsoc.2025.117777
Received 29 May 2025; Received in revised form 15 August 2025; Accepted 25 August 2025
Available online 27 August 2025

they provide support for cell growth and tissue-like structure formation [9], bone healing processes [10], and controlled drug release [11].

Scaffolds can be prepared into green bodies via various techniques, with robocasting being one of them. The robocasting technique relies on the formulation of glass loaded inks which can be extruded through nozzles. The first development of this technique relied on manipulating the interparticle forces within the particle loaded suspension to create inks with the correct rheological properties for printing [12]. An ideal ink should be easily mixable, support high glass powder loadings while retaining printable viscosity. Additionally, it should have pseudoplastic behavior for precise extrusion. It must exhibit adequate yield strength to endure the mechanical load of multiple scaffold layers. The ink should be biocompatible, with a degradation rate aligned with the pace of tissue regeneration, and capable of adhering to target surface for stable integration. Additionally, it must maintain structural integrity under physiological conditions, be sterilizable, and scalable for clinical applications. Robocasting is the most used 3D printing technique for bioactive glasses due to the speed of fabrication, the ease at which inks can be produced and the capability and accessibility of the machines. The ink also comes with a binder, formulated with the correct rheological properties to act as a carrier of the particles, which binds them together into the desired architecture. Pluronic F-127, often used as the binder, is a block co-polymer surfactant with thermally reversable rheological behavior, that can be dissolved in water, forming a stable suspension via steric repulsion of the –OH groups [13–15]. Due to its thermally reversible properties, Pluronic F-127 enables easy mixing of glass particles at low temperatures while enabling the formation of high modulus and high stiffness pseudoplastic inks at room temperature [16]

To be considered as suitable candidate as implant, the scaffold should feature various properties [17]: the primary requirement is biocompatibility, ensuring that cells adhere, function, migrate, and proliferate without triggering a significant immune response that could hinder healing or cause rejection. The scaffold must also be biodegradable and non-toxic. Adequate pore size is essential for effective cell migration and binding. In addition to these biological considerations, the scaffold must exhibit mechanical characteristics that align with the biomechanical demands of the target implantation site and must be sufficiently robust to permit surgical handling during implantation. After implantation, the scaffold must also present negligible immune reaction to reduce inflammatory response.

Due to their porous structure, scaffolds have demonstrated potential for use in targeted drug delivery systems which is a fairly recent field in pharmacy that focuses on creating advanced systems to deliver drugs more effectively and safely. Nowadays, these systems have been used to deliver *in-situ* light-regulated agents, which are compounds that react to light [18,19], or to reversibly photoisomerize photoswitchable drugs to their pharmacologically active conformation (photopharmacology) [20]. The M_2 muscarinic acetylcholine receptor (mAChR) is a promising target for dualsteric modulators, that engage both the orthosteric site (where acetylcholine binds) and an allosteric site on the receptor. This dual engagement offers more refined control over the receptor's function, which is critical to regulate heart rate and various central nervous system activities associated to M_2 mAChRs [21]. For instance, a dualsteric modulator could be designed to selectively enhance or inhibit M_2 receptor activity in specific tissues, providing therapeutic benefits in conditions like cardiac arrhythmias or neurological disorders without affecting other targets, including muscarinic receptor subtypes [22,23]. PAI (Phthalimide Azobenzene Iperoxo) is a photoswitchable dualsteric modulator that can effectively activate M_2 mAChRs in its dark-adapted (*trans*) form. Its activity can be reversibly switched off and on using 365 nm (*cis*-PAI) and 460 nm (*trans*-PAI), respectively [24]. However, the need for ultraviolet (UV) and visible light to switch PAI limits its use *in-situ* as these wavelengths do not penetrate deeply into tissue, due to scattering and optical absorption [25]. PAI can be activated with IR light using pulsed lasers (two- [24] and three-photon excitation [26]) but these devices are not portable.

Photon upconversion (UC) is a nonlinear optical process that converts two or more low-energy photons into a single high-energy photon [27,28]. In this way, 980 nm, which is tissue-transparent, can be converted into visible photons. Upconverter materials have shown significant potential in various fields due to their unique optical properties, including bioimaging, *in vitro* detection and imaging [29,30]. Recently, Ghanavati et al. demonstrated the successful preparation of a biophotonic scaffold codoped with Yb^{3+} and Er^{3+} able to emit green light under 980 nm pumping, the brightness of which was sufficient to release nitric oxide [31]. However, there is a major limitation of this approach to obtain green light using 980 nm pumping which is the continuous requirement of an external pump source to sustain the green emission. Constant external excitation can be impractical for *in-vivo* applications, particularly in controlled drug release systems.

In contrast to the upconversion process, the persistent luminescence (PeL), or afterglow, refers to the emission that continues even after the excitation source is removed. The duration of PeL emission varies depending on the composition of the luminescent material and the ambient temperature, ranging from a few seconds to several hours [32]. Among PeL phosphors, $SrAl_2O_4$: Eu^{2+}, Dy^{3+} is recognized as one of the most efficient long-lasting emitters, capable of exhibiting a strong green afterglow for up to 20 h following charging [33]. Despite their advantages, the primary limitation of PeL phosphors in biomedical applications is their dependence on UV or blue light for charging and restricts their use in deep-tissue applications since short wavelength radiation does not penetrate biological tissues effectively. As a result, these phosphors must be pre-charged before implantation. To address this challenge, some studies demonstrated that green afterglow can be obtained after NIR charging by integrating Yb^{3+} and Tm^{3+} ions with $SrAl_2O_4$: Eu^{2+}, Dy^{3+} [34–36]. It is the blue upconversion emission from the Tm^{3+} ions obtained under 980 nm pumping which can be used to charge the PeL phosphors (i.e. to induce charge trapping), eventually leading to green afterglow upon NIR charging. However, the blue emission from the UC particles needs to be strong enough in order to sufficiently charge the $SrAl_2O_4$: Eu^{2+}, Dy^{3+} phosphors.

Despite of being bioactive, phosphate glasses are also good hosts to incorporate rare-earth ions. However, the phonon energy of those glasses is rather high, leading to low upconversion efficiencies [8,37]. On the other hand, crystals with low phonon energy exhibit higher absorption and emission cross-sections compared to glasses, allowing a more efficient energy transfer (ET), achieving higher upconversion efficiency [38]. Calcium tungstate ($CaWO_4$) is a promising material for upconversion applications. When codoped with Tm^{3+} and Yb^{3+}, this crystal shows intense blue upconversion emissions at 473 nm under 980 nm excitation, due to the $^1G_4 \rightarrow {}^3H_6$ transition of Tm^{3+} ions [39]. There are a few advantages using $CaWO_4$ crystals as blue upconverter such as facile fabrication conditions via solid-state synthesis, high activator concentrations, and intrinsic sensitization of lanthanide ions through a ligand-to-metal charge transfer and it does not interfere with the bioresponse of scaffolds [31,40]. This material also exhibits good thermal stability, making it suitable for applications in high-temperature environments [41], and is known to be beneficial in applications such as photocatalysis and phototherapy [42].

In this paper, a 3D printed porous scaffold is developed, composed of the bioactive phosphate glass with the composition (in mol%) 45 P_2O_5 – 20CaO - 10MgO – 10SrO – 10Na_2O – 2.5B_2O_3 – 2.5SiO_2 mixed with $CaWO_4$:Tm^{3+},Yb^{3+} crystals and $SrAl_2O_4$: Eu^{2+}, Dy^{3+} phosphors. Challenges in the sintering process of the composite scaffold are discussed. A proof of concept on a controlled in-situ drug activation from the biophotonic scaffold utilizing NIR is presented.

2. Materials and Methods

2.1. Scaffold preparation

The 45 P_2O_5 – 20CaO - 10MgO – 10SrO – 10Na_2O – 2.5B_2O_3 –

2.5SiO_2 (in mol%) glass was prepared using standard melt quenching process using platinum crucible as in [8]. The raw materials were $NaPO_3$ (Alfa Aesar, tech.), H_3BO_3 (Sigma-Aldrich, ≥99.5 %), SiO_2 (Umicore, 99.99 %), $SrCO_3$ (Sigma-Aldrich, ≥98 %), NH_6PO_4 (Sigma-Aldrich, ≥99.5 %) and MgO (Honeywell, ≥99 %). The $Ca(PO_3)_2$ was synthesized using $CaCO_3$ (AlfaAesar, >99 %) and $NH_4H_2PO_4$ (Sigma-Aldrich, >99 %). A glass batch of 30 g was introduced into the furnace at room temperature and gradually heated at a rate of 10 °C/min until reaching 1000 °C, where it stayed for 1 h. Following quenching, the glass underwent annealing at 425 °C for 8 h. Subsequently, the amorphous glass was ball milled and sieved to obtain particles smaller than 38 μm.

$CaWO_4$:Yb^{3+},Tm^{3+} crystals were prepared via solid-state reaction, with 0.5 mol% of Tm_2O_3 and 15 mol% of Yb_2O_3. The trivalent dopants substituting divalent host ions Ca^{2+} were compensated for charge with monovalent Na^+ with equal percentage as both trivalent dopants as in [43]. The raw materials were $CaCO_3$ (Alfa-Aesar, technical grade), Na_2CO_3 (Sigma-Aldrich, 99,9 %), WO_3 (Honeywell-Fluka, 99 %), Yb_2O_3 (Sigma-Aldrich, 99.9 %) and Tm_2O_3 (Sigma-Aldrich, 99.9 %). The chemicals were mixed and heated at 1200 °C for 4 h using a 3 °C/min heating rate in ambient atmosphere in a furnace. Finally, the crystals were manually crushed and then ball milled for 3 min using a planetary ball mill (Fritsch GmbH, Idar-Oberstein, Germany) to minimize the clogging during the printing process.

The scaffolds were fabricated using the robocasting technique using 3Dn-Tabletop robocasting machine (nScrypt Inc., Orlando, FL, USA). The ink was prepared by manually mixing bioactive glass powder with 5 wt% of $CaWO_4$: Yb^{3+}, Tm^{3+} crystals and 5 wt% of commercial $SrAl_2O_4$:Eu^{2+},Dy^{3+} (PYG-6L, Realglow®). This mixture was combined with a water-based polymeric binder solution containing 30 wt% Pluronic F-127, resulting in a final ink composition of 30 vol% solid powder and 70 vol% binder solution. The prepared ink, with a total volume of 2 cm^3, was loaded into a plastic cartridge and left to stabilize for an hour before the printing process Scaffolds with a diameter of 3.3 mm were fabricated by depositing parallel printed lines with an interlayer spacing of 0.3 mm, resulting in a total height of 3.7 mm. The structure was constructed by alternating the printing direction with a 90° rotation between successive layers. As in [8], the 3D printed scaffolds were subsequently air-dried at ambient temperature and finally sintered at 525 °C at a rate of 5 °C/min for 1 h using a furnace (Nabertherm LT 9/11/SKM electric muffle furnace) to fuse the glass particles and to remove the binder.

A solution composed by PAI (10 μM) dissolved in Milli-Q water was deposited as a thin film in contact with the 3D printed scaffold and exposed to 980 nm irradiation (Roithner Lasertechnik GmbH, model RLDH980–160–3, 160 mW). Absorbance measurements were recorded every 15-minutes over a duration of 45 min to evaluate changes induced by the interaction between PAI and the scaffold under NIR illumination. The experimental protocol comprised three distinct conditions: 1) Dark condition (baseline absorbance): PAI in its *trans* (active) configuration was maintained in a light-free environment to establish its active baseline absorbance profile. 2) PAI was irradiated with UV light for 30 min to facilitate transition to its inactive *cis* form to establish its inactive baseline absorbance profile. 3) PAI, in contact with the scaffold, was exposed to 980 nm irradiation, and its absorbance was measured in a regular interval of time until full photoisomeration was achieved. To understand the contribution from each active crystal in the activation of the molecule, the same experimental conditions were performed using scaffolds prepared only with $CaWO_4$: Yb^{3+}, Tm^{3+} crystals and only with $SrAl_2O_4$:Eu^{2+},Dy^{3+} phosphors.

2.2. Characterization

A Micro-X Ray Fluorescence (XRF) Spectrometer (Bruker Tornado Plus) was used for element mapping. The measurement was carried out under vacuum atmosphere at room temperature.

SEM-EDX-CL measurements were conducted under low vacuum (20 Pa) and 20 kV using a Hitachi (Hitachi High-Technologies Co. Ltd., Tokyo, Japan) S-3400N scanning electron microscope (SEM), equipped with a Thermo Scientific (Thermo Fisher Scientific Inc., Waltham, MA, USA) Noran System 7 energy-dispersive X-ray detector (EDX) for chemical analysis. Cathodoluminescence (CL) was collected using an optical fiber and analyzed using a CCD (Princeton Instruments ProEM 16002), attached to a spectrograph (Princeton Instruments Acton SP2358).

The upconversion spectra of the glasses were recorded using a TEC-cooled fiber-coupled multimode laser (II-VI Laser enterprise), with λ_{exc} ~ 975 nm, delivering ~ 300 mW with a spot size of approximately 2 mm. The emission spectra were recorded in a range of 400–750 nm using a Spectro 320 optical spectrum analyzer (Instrument Systems Optische Messtechnik GmbH, Germany). The absolute upconversion intensity was measured using a Hagner ERP-105 photometer equipped with an SD27 photopic luminance detector. The emission was induced by a Thorlabs MCLS1–980–20 980 nm laser operating at full power (200 mW, spot size of 0.25 mm2). Both the excitation source and the detector were positioned 5 mm away from the sample surface. The measurements were carried out at room temperature, and the sample was crushed into a powder to allow for a consistent basis for comparing emission intensities.

The persistent luminescence (PeL) spectra of the samples were acquired with a Varian Cary Eclipse Fluorescence Spectrophotometer equipped with a Hamamatsu R928 photomultiplier tube (PMT). The measurements were performed at room temperature. The samples, crushed into powder to enable comparison of their PeL intensity, were irradiated for 5 min with a hand-held 254 nm UV lamp (UVGL-25, 4 W). Their PeL spectra were collected one minute after stopping the irradiation. The detector parameters were Bio-/chemiluminescence mode, scan range 400—1000 nm, emission slit 20 nm, data interval 1 nm, PMT voltage 600 V (medium). The PeL decay curve measurements were conducted by irradiating the powdered sample for 5 min with a 254 nm hand-held UV-lamp (UVGL-25), after which the luminance values were obtained after which the luminance values were obtained by taking a measurement every second starting 1 s after stopping the irradiation. The equipment consisted of Hagner ERP-105 luminance meter coupled with a Hagner SD 27 detector. The PeL decay after 5 min of irradiation with a 980 nm laser (200 mW) focused on 2.5 mm^2 (8 W/cm2), was recorded using an ILT 1700 calibrated photometer (International Light Technologies) equipped with a photopic filter (YPM). For these measurements a thick metal plate with a circular hole (Ø 5 mm) was inserted between the sample (bulk form) and the detector to minimize effects from variations in sample size and morphology. The photoluminescence (PL) spectra (λ_{exc}: 266 nm, Nd:YAG pulse laser, 8 ns, TII Lotis) were measured at room temperature using an Avantes CCD spectrometer (AvaSpec-2048 ×14).

The absorbance spectra of the PAI molecules in contact with the scaffolds were measured using a Shimadzu UV-1800 UV–VIS Spectrophotometer with standard quartz cuvettes (10 mm light path).

3. Results and discussion

The $CaWO_4$: Yb^{3+}, Tm^{3+} crystals were prepared using a solid-state reaction. As shown in Figure S1a, this method leads to crystals with an irregular morphology and grain size due to the restricted diffusion during the synthesis [44]. Due to risk related to nozzle clogging during the robocasting process, the size of the crystals was reduced using a planetary ball mill. As expected, the crystals size is progressively reduced from ~ 30 μm to ~2 μm when ball milled up to 20 min. However, ball milling process can lead to amorphization or crystalline phase changes as explained in [45]. Here, no changes in the XRD pattern of the crystals were observed after ball milling for up to 20 min as shown in Figure S1b. The XRD pattern of the crystal before and after ball milling exhibits the same peaks which correspond to those of the $CaWO_4$: Yb^{3+}, Tm^{3+} crystals [ICDD: 04–008–6874] representing Scheelite-type tetragonal structure [46]. However, the milling process

leads to a reduction in intensity of the blue upconversion emission under 980 pumping, most likely due to the creation of defects that decrease the efficiency of energy transfer between the rare earth ions as suggested in [47]. Indeed, the formation of defects can make non-radiative transitions more likely to occur, limiting the excited state lifetime (for the intermediate states of Tm^{3+}), thus reducing the probability for the energy transfer from Yb^{3+} to the Tm^{3+} in this intermediate state leading to weaker UC emission intensities as shown in Figure S1c. Therefore, crystals ball milled for 3 min were used for the synthesis of the scaffold.

In order to maintain the mechanical properties comparable to the bone mineral phase, the concentration of $CaWO_4$:Yb^{3+},Tm^{3+} and $SrAl_2O_4$:Eu^{2+},Dy^{3+} within the scaffold matrix should be limited to 10 wt

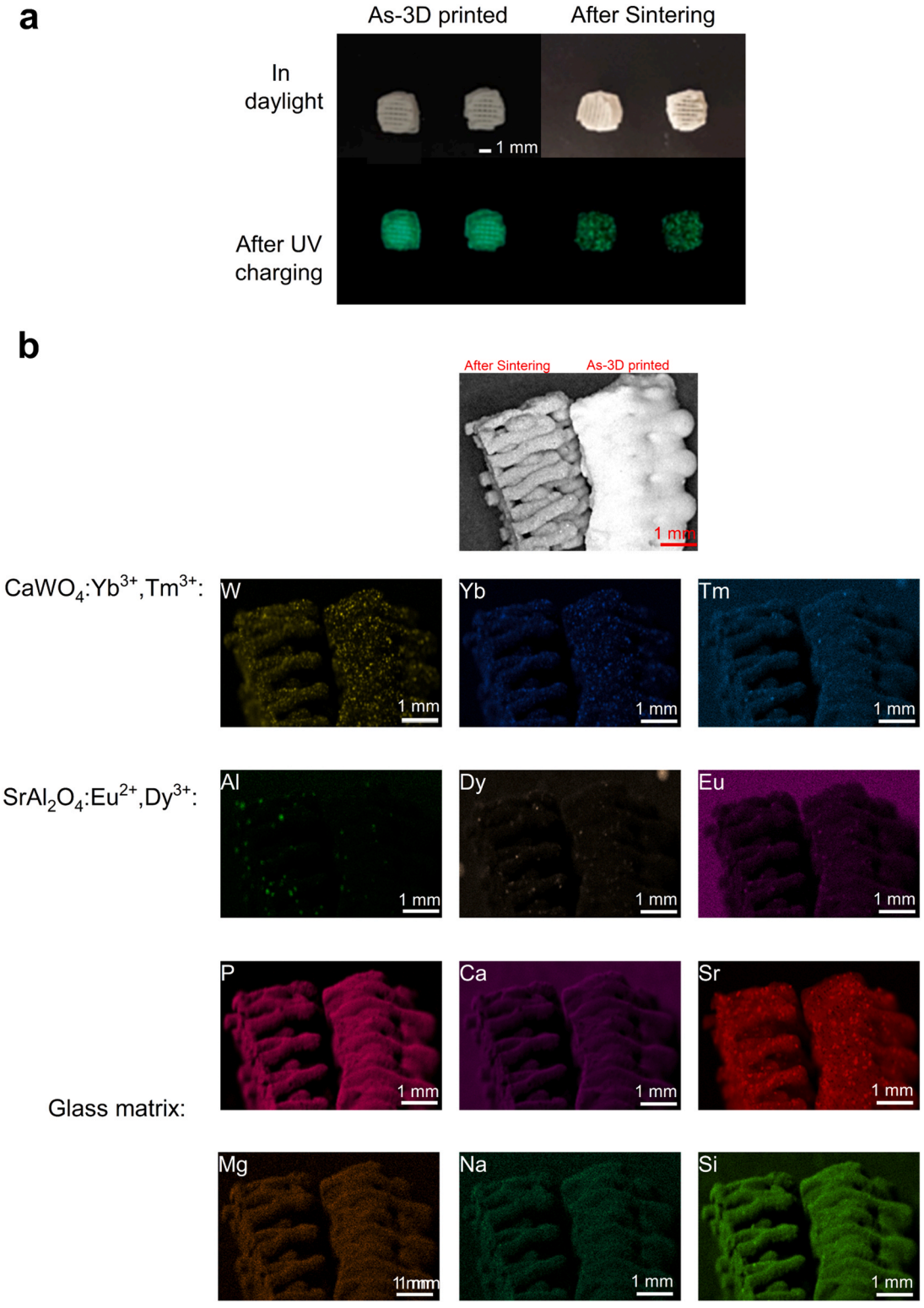

Fig. 1. (a) Pictures in daylight and after UV charging of the as-3D printed and sintered scaffolds, one should notice that the true body color of the sintered scaffold is not properly represented due to different illumination. (b) XRF elemental mapping of the as-3D printed and sintered scaffolds.

% as explained in [31]. Thus, scaffolds were fabricated with 5 wt% of $CaWO_4$:Yb^{3+},Tm^{3+} and 5 wt% of $SrAl_2O_4$:Eu^{2+},Dy^{3+} as this ratio was found to be the most promising ratio for efficient charging of the PeL phosphors by the blue UC crystals using 980 nm charging as depicted in Figure S2.

Following the robocasting process, the scaffolds were sintered to completely remove the binder and to promote densification of the scaffold structure. The sintering process led to a progressive reduction in porosity through the formation of solid necks between adjacent particles, promoting particle coalescence and a consequent decrease in overall pore volume, ultimately yielding a dense microstructure with minimal voids. The sintering also leads to residual carbon from the binder, that is not fully decomposed, which leads to a light grey coloration as shown in the Fig. 1**a**. All scaffolds emit green afterglow after being charged with the UV lamp indicating that the $SrAl_2O_4$:Eu^{2+},Dy^{3+} phosphors survive the robocasting and sintering processes. The presence of the $CaWO_4$:Yb^{3+},Tm^{3+} and of $SrAl_2O_4$:Eu^{2+},Dy^{3+} was confirmed using XRF (Fig. 1**b**). Elemental mapping of the as-printed scaffold revealed a homogeneous distribution of the glass, $CaWO_4$:Yb^{3+},Tm^{3+} and $SrAl_2O_4$:Eu^{2+},Dy^{3+}, with no appreciable changes observed in their spatial distribution following sintering.

A decrease in the intensity of the afterglow after sintering is clearly visible in Fig. 1**a**. Therefore, the PeL and PL spectra of the scaffolds were measured before and after sintering in order to verify the impact of the sintering on the spectroscopic properties of the $SrAl_2O_4$:Eu^{2+},Dy^{3+} phosphors embedded in the scaffold. The PeL and PL spectra, presented in Fig. 2**a** and **b** respectively, exhibit a band which can be related to the 4 $f^6 5d^1 \rightarrow 4\ f^7$ transition of Eu^{2+} [48]. While no changes in the shape of the emission bands are seen, a significant reduction in the intensity of the PeL and PL emissions is observed after sintering. This suggests that the thermal process has no impact on the Eu^{2+} sites in the $SrAl_2O_4$:Eu^{2+}, Dy^{3+} but is suspected to modify the defect-related traps, structural ordering, and microstructural properties in the PeL phosphors [49]. A decrease in the capacity for charge carrier storage is expected to occur due to the sintering process, resulting in a shorter afterglow duration. Also, the greyish body color of the sintered scaffolds is suspected to be detrimental, as less infrared radiation is available for the upconversion process reducing the intensity of the blue UC emission reaching the $SrAl_2O_4$:Eu^{2+},Dy^{3+} particles. It is also possible that the afterglow has difficulties escaping the material. All these effects primarily impact defect-related charge storage mechanisms rather than altering Eu^{2+} sites, leading to reduced radiative recombination efficiency and to increased competition from non-radiative processes [49].

Fig. 2**c** shows the SEM image of the as-3D printed and sintered scaffolds. At first sight, it is difficult to distinguish the glass particles from the $CaWO_4$:Yb^{3+},Tm^{3+} and $SrAl_2O_4$:Eu^{2+},Dy^{3+} in the backscattered electron image, although bright spots can clearly be seen in the image, revealing parts of the scaffold made from atoms with higher atomic number. In order to locate the various materials in the scaffolds, the EDX elemental maps and cathodoluminescence (CL) spectra were recorded using 20 kV accelerating voltage to have high CL and EDX intensity, while maintaining reasonably high spatial resolution. Based on the EDX maps (Fig. 2**d**), the brightest spots in the BSE images are thought to be the $CaWO_4$:Yb^{3+},Tm^{3+} crystals, while the glass particles appear darker. The $SrAl_2O_4$:Eu^{2+},Dy^{3+} phosphors are bigger and partially covered by the scaffold material. Looking at the Al elemental map, the position of the $SrAl_2O_4$:Eu^{2+},Dy^{3+} phosphors can be revealed. The areas with high intensity of emission (Fig. 2**e**) align with the position of the $SrAl_2O_4$:Eu^{2+}, Dy^{3+} phosphors. The emission spectra (Fig. 2**e, top**) taken at such a position exhibits a broad emission band with high intensity and centered at 545 nm. This emission band can be related to the $4f^6 5d^1 \rightarrow 4f^7$ transition of Eu^{2+}. At locations where the $CaWO_4$:Yb^{3+},Tm^{3+} crystals are suspected, there are additional contributions at 475 nm and 645 nm which can be related to the $^1G_4 \rightarrow {}^3H_6$, and $^1G_4 \rightarrow {}^3F_4$ transitions of Tm^{3+}. A strong emission band can also be seen at around 800 nm, which can be assigned to $^3H_4 \rightarrow {}^3H_6$ transition of Tm^{3+}. The presence of the $CaWO_4$:Yb^{3+},Tm^{3+} crystals in the scaffold is also confirmed from the ratio of the emission in the 785 – 815 nm to the total emission intensity in each pixel (Fig. 2**e, bottom right**). It is important to point out that no clear changes in the distribution of $CaWO_4$:Yb^{3+},Tm^{3+} and $SrAl_2O_4$:Eu^{2+},Dy^{3+} within the scaffolds and in their emission spectra can be observed after the sintering process, confirming that the sintering process does not lead to, e.g., crystals decomposition or oxidation of the Eu dopant.

The sintering process has also an impact on the upconversion properties. As shown in Fig. 3, the intensity of the emissions at 475 nm and at 690 nm, corresponding to the $^1G_4 \rightarrow {}^3H_6$ transition and to the $^3F_{2,3} \rightarrow {}^3H_6$ transition of Tm^{3+} respectively, decreases probably due to the formation of internal/surface crystalline defects as explained in [50] and also probably due to the greyish coloration that reduces the number of NIR photons reaching the $CaWO_4$:Yb^{3+},Tm^{3+} crystals. Given the power dependency of the UC process, in the case of three NIR photons, a reduction of the scaffold transmission by a factor of 2, would lead to a reduction in UC emission of 8. It is interesting to point out that the decrease in the intensity of the emission at 690 nm is less than for the emission at 475 nm. The sintering process is expected then to deplete the $^3H_4$ level, reducing the conversion to blue-emitting state $^1G_4$ while increasing the $^3F_4$ population. This, in turn, increases the energy transfer from Yb^{3+} to the red-emitting $^3F_{2,3}$ level [51]. A similar effect was reported in [52]. The quantification of the upconversion emission was measured under 980 nm pumping (200 mW, and spot size of 0.25 mm^2). The as-3D printed scaffold exhibits 1218 mcd/m^2 of luminance which decreases to 261 mcd/m^2, being visible by naked eye in both cases.

The PeL decay after 980 nm illumination was measured before and after sintering (Fig. 4). After being charged with 980 nm (8 W/cm^2 irradiance) for 5 min, the as-3D printed scaffolds emit green light well above the standard threshold of the practical limit of visibility set at 0.3 mcd/m^2 [53] for over 15 min. The video of the green afterglow after NIR charging from the as-3D printed scaffold can be found in Video S1. As shown in Fig. 4, the maximum luminance from the sintered scaffold is measured at ~0.3 mcd/m^2. This loss in the PeL properties after sintering can be related to the decrease in intensity of the blue UC and most probably also due to the greyish coloration of the scaffold after sintering.

Due to the decrease in intensity of the blue emission under 980 nm pumping after sintering, the photoisomerization of the PAI molecule upon 980 nm light stimulus was conducted using the as-3D-printed scaffold. For this experiment, a different 980 nm continuous-wave laser was employed. Its output power was insufficient to obtain green afterglow after NIR charging. Nonetheless, the scaffold was placed in contact with the *cis*-PAI isomer (pharmacologically inactive form obtained by preirradiation with 365 nm light) and was irradiated with a 980 nm laser for up to 45 min. The PAI absorbance spectrum was measured every 15 min during the irradiation treatment. As depicted in Fig. 5**a**, the absorbance spectra exhibit an absorbance band centered at 310 – 320 nm, the intensity of which changes due to *cis-trans* photoisomerization. Low and high absorption in the plot correspond to *cis* and *trans* isoforms, respectively [24]. The relative absorbance, presented in the Fig. 5**b,** is calculated by normalizing the change in absorbance at time t to the total change between the active state and the UV-exposed state (from the dark state to 45 min of irradiation by the 980 nm laser) using the following equation:

$$A_{relative} = \frac{A_\lambda(active) - A_t}{A_\lambda(active) - A_\lambda(UV)} \quad (1)$$

where $A_\lambda(active)$ is the absorbance measured in the absence of UV light (baseline or initial state), A_t is the absorbance at a given time t and $A_\lambda(UV)$ is the absorbance after full UV exposure.

Under 980 nm pumping, a progressive increase in the intensity of the absorption band is observed, suggesting a progressive photo-induced isomerization from *cis* (inactive) to *trans* (active) form. However, under 980 nm pumping, this scaffold exhibits both the blue upconversion emission from the $CaWO_4$: Yb^{3+}, Tm^{3+} crystals and the green

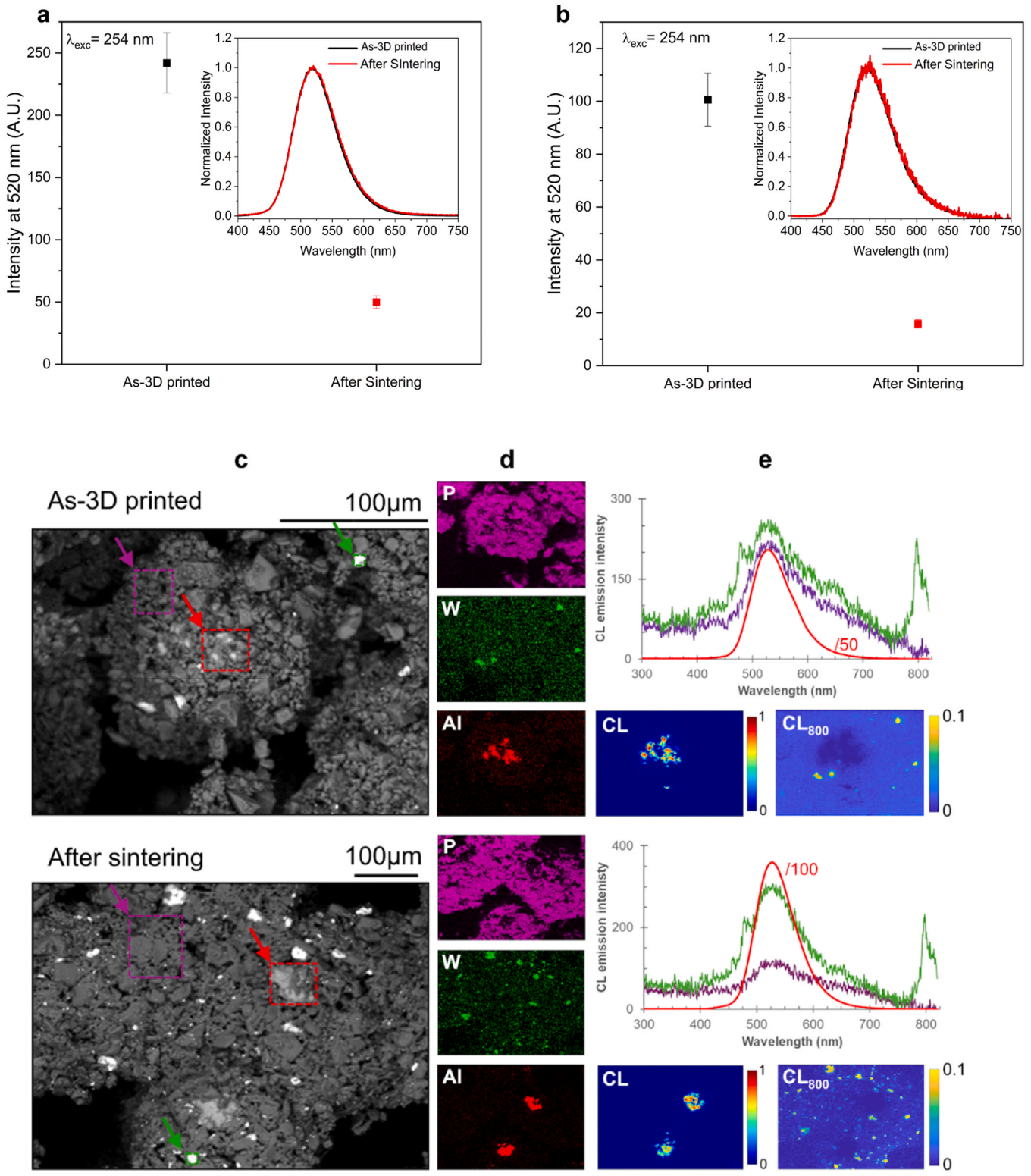

Fig. 2. (a) PeL spectra of the as-3D printed and sintered scaffolds (λ_{exc}= 254 nm) (b) Steady-state PL spectra of the as-3D printed and sintered scaffolds (λ_{exc}= 254 nm) (c) SEM Backscattered electron (BSE) image of the cross-section of the as-3D printed and sintered scaffolds and their corresponding (d) EDX maps for P, W and Al, being illustrative for the distribution of the scaffold material, the $CaWO_4$ crystals and the $SrAl_2O_4$ PeL particles, respectively. (e) Top: CL emission spectra for the areas indicated in part (c). Bottom left: total intensity map. Bottom right: fraction of the emission in the wavelength range from 785 nm to 815 nm, with respect to the total emission intensity from 400 nm to 815 nm.

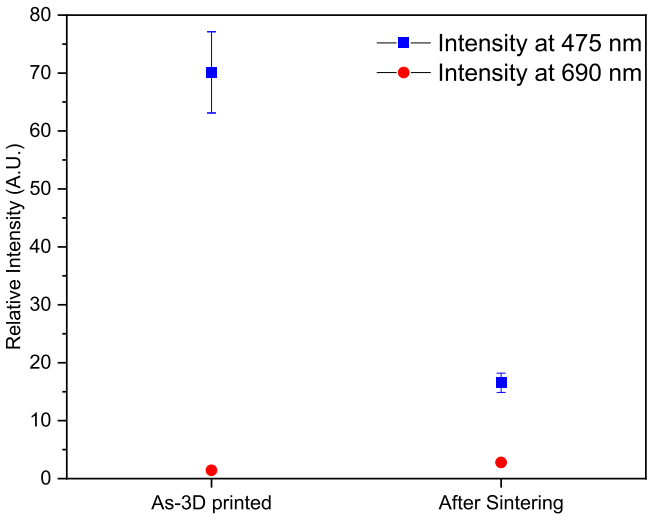

Fig. 3. Relative intensity of the emissions at 475 and 690 nm from the scaffolds before and after sintering (λ_{exc}= 980 nm).

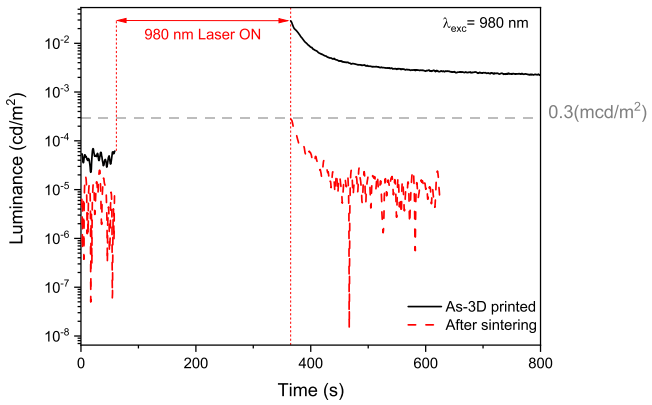

Fig. 4. – Decay curve of the visible emission for the as-3D printed and sintered scaffolds after being charged for 5 min at 980 nm (power density).

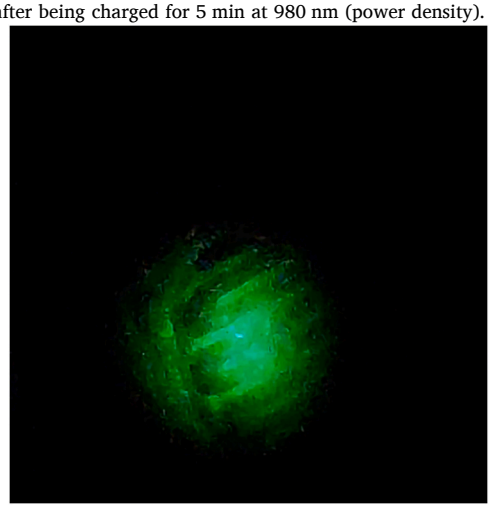

Video S1. A video clip is available online. Supplementary material related to this article can be found online at doi:10.1016/j.jeurceramsoc.2025.117777.

emission from the $SrAl_2O_4$:Eu^{2+},Dy^{3+} phosphors. Although cis-trans PAI isomerization is optimally driven by 460 nm blue light, both emissions probably contribute to the photoactivation of the molecule, making it challenging to distinguish the role of $CaWO_4$: Yb^{3+}, Tm^{3+} crystals from the role of $SrAl_2O_4$:Eu^{2+},Dy^{3+} phosphors on the photo-induced isomerization process. To address this, two scaffolds were prepared using the same 3D printing process; one with only $CaWO_4$: Yb^{3+}, Tm^{3+} crystals (5 wt%) and the other one with only $SrAl_2O_4$:Eu^{2+},Dy^{3+} phosphors (5 wt%). As shown in Fig. 5**c** and **d**, an increase in the intensity of the absorption band is seen when irradiating the $CaWO_4$: Yb^{3+}, Tm^{3+} crystals containing scaffold emitting only the blue light under 980 nm pumping. In contrast, the scaffolds containing only $SrAl_2O_4$:Eu^{2+},Dy^{3+} did not show the ability to induce the photoisomerization after being charged with UV for 45 min (Fig. 5**e**) and maintained high levels of *cis* isomerization with no significant shift toward the *trans* form (Fig. 5**f**). Therefore, the photoisomerization of *cis*-PAI to *trans*-PAI is mainly obtained from blue light emission of the $CaWO_4$: Yb^{3+}, Tm^{3+} crystals, in agreement with the absorption spectrum of *cis*-PAI and the known optimal isomerization at 460 nm [26].

4. Conclusion

In the present work, $CaWO_4$:Yb^{3+},Tm^{3+} crystals and $SrAl_2O_4$:Eu^{2+}, Dy^{3+} phosphors were effectively incorporated into a 3D printed bioactive phosphate scaffold prepared using robocasting method. After charging with 980 nm, the as-3D printed scaffold emits a green afterglow for ~15 min above the threshold level of 0.3 mcd/m^2 due to the blue emission from the $CaWO_4$ crystals co-doped with Yb^{3+} and Tm^{3+} which charges the $SrAl_2O_4$:Eu^{2+}, Dy^{3+} phosphors. After sintering, green afterglow with low intensity was observed from the scaffold after charging with 980 nm probably due to the formation of defects in the $CaWO_4$: Yb^{3+}, Tm^{3+} crystals, which hampered strong blue UC emission. Nonetheless, the emission from the as-prepared scaffolds under 980 nm pumping was found to be sufficient to photoisomerize PAI and convert the compound from its pharmacologically inactive *cis* form intro the active *trans* isomer.

Our findings clearly demonstrate that the newly developed scaffolds could be used as light-emitting implants in the body at sites where localized and on-demand drug action is required, for example in the region around a resected tumor to avoid relapse [55], attached to the heart as a pacemaker [24], in the spinal cord to inhibit pain [56], or in the brain cortex to enhance activity [54] or to inhibit seizures [57]. These implants would be combined with NIR illuminators operated externally to activate systemically administered photoswitchable drugs. For that purpose, our next steps will be to optimize the biocompatibility of these materials and to test their preclinical safety.

CRediT authorship contribution statement

Nirajan Ojha: Writing – review & editing, Writing – original draft, Validation, Methodology, Formal analysis, Conceptualization. **Magalhaes Evellyn:** Writing – review & editing, Writing – original draft, Methodology, Formal analysis, Data curation, Conceptualization. **Laeticia Petit:** Writing – review & editing, Writing – original draft, Validation, Supervision, Project administration, Funding acquisition, Formal analysis, Conceptualization. **Mika Lastusaari:** Writing – review & editing, Validation, Methodology, Formal analysis. **Philippe F. Smet:** Writing – review & editing, Writing – original draft, Validation, Methodology, Formal analysis. **Ekin Opar:** Writing – review & editing, Validation, Methodology, Formal analysis. **Sonya Ghanavati:** Writing – review & editing, Methodology, Formal analysis, Data curation. **Pau Gorostiza:** Writing – review & editing, Writing – original draft, Validation, Conceptualization, Methodology, Funding acquisition, Formal analysis. **Jonathan Massera:** Writing – review & editing, Validation, Conceptualization, Supervision, Methodology, Formal analysis. **Carlo Matera:** Writing – review & editing, Validation, Methodology, Formal analysis. **Fabio Riefolo:** Writing – review & editing, Validation, Methodology, Formal analysis.

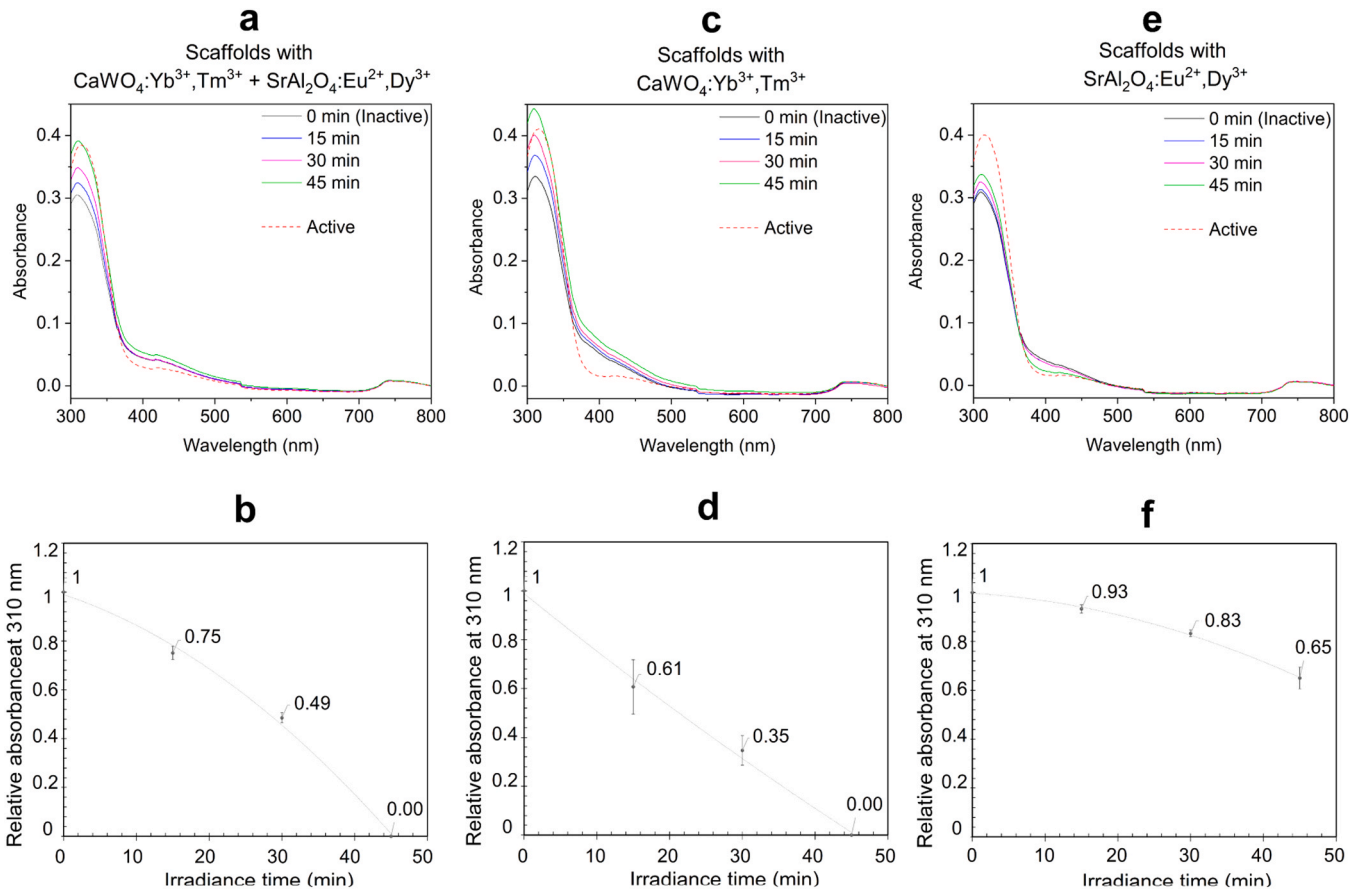

Fig. 5. Absorbance spectra measured at different illumination conditions using 980 nm pumping and their corresponding relative absorbance when PAI is in contact with scaffold containing $CaWO_4:Yb^{3+},Tm^{3+}$ crystals and $SrAl_2O_4:Eu^{2+},Dy^{3+}$ phosphors (a and b, respectively) and with scaffold containing only $CaWO_4:Yb^{3+},Tm^{3+}$ crystals (c and d, respectively) Absorbance spectra measured at different illumination conditions using a UV light charging and their corresponding relative absorbance when PAI is in contact with scaffold containing only $SrAl_2O_4:Eu^{2+},Dy^{3+}$ phosphors (e and f, respectively). The dotted line in each graph represents the spectrum of the active trans isomer. Error bars represent the standard deviation of two independent measurements (n = 2).

Declaration of Competing Interest

The authors declare the following financial interests/personal relationships which may be considered as potential competing interests: Evellyn Santos Magalhaes reports financial support was provided by Tampere University and Tampere University of Applied Sciences. If there are other authors, they declare that they have no known competing financial interests or personal relationships that could have appeared to influence the work reported in this paper.

Acknowledgements

This work was supported by Research Council of Finland [Flagship Program, Photonics Research and Innovation PREIN-320165; MAX-HEAL project: #361159]. This research has also received funding from the European Union's HORIZON-EIC-2023 PATHFINDER- OPEN-01 programme under grant agreement No. 101130883; from the European Union's Horizon 2020 programme (the Human Brain Project SGA3, 945539 and DEEPER, 101016787); project DEEPRED with reference PID2019-111493RB-I00 funded by MICIU/AEI /10.13039/ 501100011033; project EPILLUM with reference PID2022- 142609OB-I00 funded by MICIU/AEI /10.13039/ 501100011033 and by FEDER, UE; SGR-Cat 2021 with reference 2021 SGR 01410 (AGAUR, Generalitat de Catalunya); Research Network in Biomedicine eBrains-Spain, RED2022–134823-E. IBEC is a recipient of the Severo Ochoa Award of Excellence from MICIU. E. O. is supported by the FPI fellowship PRE2020–092901 financed by MICIU/AEI. P. F. S. acknowledges the Research Fund at Ghent University (BOF grant bof/baf/4y/2024/01/ 037).

Appendix A. Supporting information

Supplementary data associated with this article can be found in the online version at doi:10.1016/j.jeurceramsoc.2025.117777.

References

[1] K. Schuhladen, A.R. Boccaccini, Bioactive glass variants for tissue engineering: from the macro- to the nanoscale. in: Bioceramics, Elsevier, 2021, pp. 353–373, https://doi.org/10.1016/B978-0-08-102999-2.00015-6.
[2] M. Cannio, D. Bellucci, J.A. Roether, D.N. Boccaccini, V. Cannillo, Bioactive glass applications: a literature review of human clinical trials, Mater 14 (2021) 5440, https://doi.org/10.3390/ma14185440.
[3] L.L. Hench, Bioceramics: from concept to clinic, J. Am. Ceram. Soc. 74 (1991) 1487–1510, https://doi.org/10.1111/j.1151-2916.1991.tb07132.x.
[4] Ö.H. Andersson, I. Kangasniemi, Calcium phosphate formation at the surface of bioactive glass in vitro, J. Biomed. Mater. Res. 25 (1991) 1019–1030, https://doi.org/10.1002/jbm.820250808.
[5] T. Kondo, K. Otake, H. Kakinuma, Y. Sato, S. Ambo, H. Egusa, Zinc- and fluoride-releasing bioactive glass as a novel bone substitute, J. Dent. Res. 103 (2024) 526–535, https://doi.org/10.1177/00220345241231772.
[6] N. Sharmin, C.D. Rudd, Structure, thermal properties, dissolution behaviour and biomedical applications of phosphate glasses and fibres: a review, J. Mater. Sci. 52 (2017) 8733–8760, https://doi.org/10.1007/s10853-017-0784-4.
[7] M.T. Islam, L. Macrì Pellizzeri, K.M.Z. Hossain, I. Ahmed, Effect of varying the mg with ca content in highly porous phosphate-based glass microspheres, Mater. Sci. Eng. C. 112 (2020) 110896, https://doi.org/10.1016/j.msec.2020.111668.
[8] S. Ghanavati, L. Petit, J. Massera, New Mg/Sr phosphate bioresorbable glass system with enhanced sintering properties, J. NonCryst. Solids 616 (2023) 122446, https://doi.org/10.1016/j.jnoncrysol.2023.122446.

[9] N.A. Elkasabgy, A.A. Mahmoud, Fabrication strategies of scaffolds for delivering active ingredients for tissue engineering, AAPS PharmSciTech 20 (2019) 256, https://doi.org/10.1208/s12249-019-1470-4.

[10] M.B. Sordi, A. Cruz, M.C. Fredel, R. Magini, P.T. Sharpe, Three-dimensional bioactive hydrogel-based scaffolds for bone regeneration in implant dentistry, Mater. Sci. Eng. C. 124 (2021) 112055, https://doi.org/10.1016/j.msec.2021.112055.

[11] S. Sowmya, Nanohybrid scaffold structures for smart drug delivery applications. in: Biomimetic Nanoengineered Materials for Advanced Drug Delivery, Elsevier, 2019, pp. 53–59, https://doi.org/10.1016/B978-0-12-814944-7.00004-7.

[12] I.V. Yannas, J.F. Burke, Design of an artificial skin. I. basic design principles, J. Biomed. Mater. Res. 14 (1980) 65–81, https://doi.org/10.1002/jbm.820140108.

[13] N. Dagalakis, J. Flink, P. Stasikelis, J.F. Burke, I.V. Yannas, Design of an artificial skin. Part III. Control of pore structure, J. Biomed. Mater. Res. 14 (1980) 511–528, https://doi.org/10.1002/jbm.820140417.

[14] M.G. Haugh, M.J. Jaasma, F.J. O'brien, the effect of dehydrothermal treatment on the mechanical and structural properties of collagen-GAG scaffolds, J. Biomed. Mater. Res. A 89 (2009) 363–369, https://doi.org/10.1002/jbm.a.31955.

[15] M. Bento, R. Gaddam, A. Oskoei, P. Oliveira, H. Ferreira, J.M.F. 3D printing of macro porous Sol-Gel derived bioactive glass scaffolds and assessment of biological response, Materials 14 (2021) 5946, https://doi.org/10.3390/ma14205946.

[16] A. Nommeots-Nomm, J. Massera, Glass and glass-ceramic scaffolds: manufacturing methods and the impact of crystallization on in-vitro dissolution, in: F. Baino (Ed.), Scaffolds in Tissue Engineering - Materials, Technologies and Clinical Applications, InTech, 2017, https://doi.org/10.5772/intechopen.70242.

[17] F.J. O'brien, biomaterials & scaffolds for tissue engineering, Mater. Today 14 (2011) 88–95, https://doi.org/10.1016/S1369-7021(11)70058-X.

[18] A. Karewicz, D. Lachowicz, A. Pietraszek, Photonics in drug delivery, in: J. Van Hoorick, H. Ottevaere, H. Thienpont, P. Dubruel, S. Van Vlierberghe (Eds.), Polymer and Photonic Materials Towards Biomedical Breakthroughs, Springer, Cham, 2018, https://doi.org/10.1007/978-3-319-75801-5_5.

[19] S.A. de Oliveira, R. Borges, D. dos Santos Rosa, A.C.S. de Souza, A.B. Seabra, F. Baino, J. Marchi, Strategies for cancer treatment based on photonic nanomedicine, Mater 14 (6) (2021) 1435, https://doi.org/10.3390/ma14061435.

[20] S. Sahu, A.S. Amrutha, N. Tamaoki, Controlling protein functionalities with temporal and cellular/subcellular dimensions of spatial resolution with molecular photoswitches, Med. Res. Rev. 44 (2024) 293–334, https://doi.org/10.1002/med.22106.

[21] A. Christopoulos, F. Mitchelson, Dualsteric ligands for g protein-coupled receptors: novel insights into muscarinic acetylcholine receptor pharmacology, Trends Pharmacol. Sci. 18 (12) (1997) 434–441, https://doi.org/10.1016/S0165-6147(97)01136-1.

[22] H.-C. Lee, K.T.L. Huang, X.-L. Wang, W.-K. Shen, Autoantibodies and cardiac arrhythmias, Heart Rhythm 8 (12) (2011) 1788–1795, https://doi.org/10.1016/j.hrthm.2011.06.032.

[23] E. Scarr, Muscarinic receptors: their roles in disorders of the central nervous system and potential as therapeutic targets, CNS Neurosci. Ther. 18 (5) (2012) 369–379, https://doi.org/10.1111/j.1755-5949.2011.00249.x.

[24] F. Riefolo, C. Matera, A. Garrido-Charles, A.M.J. Gomila, R. Sortino, L. Agnetta, E. Claro, R. Masgrau, U. Holzgrabe, M. Batlle, M. Decker, E. Guasch, P. Gorostiza, Optical Control of Cardiac Function with a Photoswitchable Muscarinic Agonist, J. Am. Chem. Soc. 141 (18) (2019) 7628–7636, https://doi.org/10.1021/jacs.9b03505.

[25] C. Ash, M. Dubec, K. Donne, T. Bashford, Effect of wavelength and beam width on penetration in light-tissue interaction using computational methods, Lasers Med. Sci. 32 (8) (2017) 1909–1918, https://doi.org/10.1007/s10103-017-2317-4.

[26] R. Sortino, M. Cunquero, G. Castro-Olvera, R. Gelabert, M. Moreno, F. Riefolo, C. Matera, N. Fernàndez-Castillo, L. Agnetta, M. Decker, J.M. Lluch, J. Hernando, P. Loza-Alvarez, P. Gorostiza, Three-photon infrared stimulation of endogenous neuroreceptors in vivo, Angew. Chem. Int. Ed. 62 (2023) e202311181, https://doi.org/10.1002/anie.202311181.

[27] F. Auzel, Upconversion and anti-Stokes processes with f and d ions in solids, Chem. Rev. 104 (2004) 139–174, https://doi.org/10.1021/cr020357g.

[28] B. Mehrdel, A. Nikbakht, A.Abdul Aziz, M.S. Jameel, M.A. Dheyab, P. Moradi Khaniabadi, Upconversion lanthanide nanomaterials: basics introduction, synthesis approaches, mechanism and application in photodetector and photovoltaic devices, Nanotechnology 33 (2022) 082001, https://doi.org/10.1088/1361-6528/ac37e3.

[29] Z. Gerelkhuu, Y.-I. Lee, T.H. Yoon, Upconversion nanomaterials in bioimaging and biosensor applications and their biological response, Nanomaterials 12 (2022) 3470, https://doi.org/10.3390/nano12193470.

[30] B. Zhou, B. Shi, D. Jin, X. Liu, Controlling upconversion nanocrystals for emerging applications, Nat. Nanotechnol. 10 (2015) 924–936, https://doi.org/10.1038/nnano.2015.251.

[31] H.F. Brito, J. Hölsä, T. Laamanen, M. Lastusaari, M. Malkamäki, L.C.V. Rodrigues, Persistent luminescence mechanisms: human imagination at work, Opt. Mater. Express 2 (2012) 371, https://doi.org/10.1364/OME.2.000371.

[32] M. Hasnat, V. Lahti, H. Byron, M. Lastusaari, L. Petit, Micro-luminescence measurement to evidence decomposition of persistent luminescent particles during the preparation of novel persistent luminescent tellurite glasses, Scr. Mater. 199 (2021) 113864, https://doi.org/10.1016/j.scriptamat.2021.113864.

[33] L. Hu, P. Wang, M. Zhao, L. Liu, L. Zhou, B. Li, F.H. Albaqami, A.M. El-Toni, X. Li, Y. Xie, X. Sun, F. Zhang, Near-infrared rechargeable "optical battery" implant for irradiation-free photodynamic therapy, Biomaterials 163 (2018) 154–162, https://doi.org/10.1016/j.biomaterials.2018.02.029.

[34] N.G. Arango, S. Vuori, H. Byron, D. Van der Heggen, P.F. Smet, M. Lastusaari, L. Petit, Near-infrared rechargeable glass-based composites for Green persistent luminescence, J. Alloy. Compd. 867 (2022) 167048, https://doi.org/10.1016/j.jallcom.2022.167048.

[35] E.S. Magalhães, A. Sedda, B. Bondzior, S. Vuori, D. Van der Heggen, P.F. Smet, M. Lastusaari, L. Petit, Glass-based composites comprised of $CaWO_4$:Yb^{3+},Tm^{3+} crystals and $SrAl_2O_4$:Eu^{2+},Dy^{3+} phosphors for Green afterglow after NIR charging, Ceram. Int. 49 (2023) 155, https://doi.org/10.1016/j.ceramint.2023.01.155.

[36] G.F. Morguetto, L.E.B. Tsunaki, J. Schneider, Bonding of alkaline and alkaline earth cations in Na-Ca-Sr polyphosphate glasses, Int. J. Appl. Glass Sci. 11 (2020) 58–65, https://doi.org/10.1111/ijag.13645.

[37] F. Auzel, Upconversion processes in coupled ion systems, J. Lumin 45 (1990) 341–345, https://doi.org/10.1016/0022-2313(90)90189-I.

[38] Y.L. Xu, Y.L. Wang, L.S. Shi, X. Tan, Blue upconversion luminescence in Tm^{3+}/Yb^{3+} codoped $CaWO_4$ polycrystals, Chin. Phys. Lett. 30 (2013) 084207, https://doi.org/10.1088/0256-307X/30/8/084207.

[39] T. Pier, T. Jüstel, Application of Eu(III) activated tungstates in solid state lighting, Opt. Mater. X 22 (2024) 100299, https://doi.org/10.1016/j.omx.2024.100299.

[40] J. Yang, M. Peng, S. Tan, S. Ge, L. Xie, T. Zhou, W. Liu, K. Zhang, Z. Zhang, J. Liu, J. Shi, Calcium tungstate microgel enhances the delivery and colonization of probiotics during colitis via intestinal ecological niche occupancy, ACS Cent. Sci. 9 (2023) 1327–1341, https://doi.org/10.1021/acscentsci.3c00227.

[41] L. Zhang, H. Wang, J. Liu, Q. Zhang, H. Yan, Nonstoichiometric tungsten oxide: structure, synthesis, and applications, J. Mater. Sci. Mater. Electron 31 (2020) 861–873, https://doi.org/10.1007/s10854-019-02596-z.

[42] D. Viswanath, S.-H. Shin, J. Yoo, S.E. Torregrosa-Allen, H.A. Harper, H. E. Cervantes, B.D. Elzey, Y.-Y. Won, Radiation-Induced photodynamic therapy using calcium tungstate nanoparticles and 5-Aminolevulinic acid prodrug, Biomater. Sci. 11 (2023) 6311–6324, https://doi.org/10.1039/D3BM00921A.

[43] W. Jones, Crystal effects influencing the course of organic solid state reactions: perfect, imperfect and surface effects, in: K.J. Roberts, R. Docherty, R. Tamura (Eds.), Engineering Crystallography: From Molecule to Crystal to Functional Form, Springer, Dordrecht, 2017, pp. 145–154, https://doi.org/10.1007/978-94-024-1117-1_9.

[44] C.M. Poffo, J.C. de Lima, S.M. Souza, D.M. Trichês, T.A. Grandi, R.S. de Biasi, Structural, thermal and optical study of nanocrystalline silicon produced by ball milling, J. Raman Spectrosc. 45 (2014) 1112–1118, https://doi.org/10.1002/jrs.2623.

[45] L. Wang, Y. Han, D. Wang, S. Wang, G. Lu, D. Liang, X. Wang, N. Pei, L. Gao, Hydrothermal synthesis of micrometer doping $CaWO_4$ phosphors assisted by polymerization, Mod. Phys. Lett. B 30 (2016) 1650246, https://doi.org/10.1142/S0217984916502468.

[46] P. Kaur, A. Khanna, M.N. Singh, A.K. Sinha, Structural and optical characterization of eu and dy doped CaWO4 nanoparticles for White light emission, J. Alloy. Compd. 834 (2020) 154804, https://doi.org/10.1016/j.jallcom.2020.154804.

[47] V. Havasi, D. Tátrai, G. Szabó, E. Varga, A. Erdőhelyi, G. Sipos, Z. Kónya, Á. Kukovecz, On the effects of milling and thermal regeneration on the luminescence properties of Eu^{2+} and Dy^{3+} doped strontium aluminate phosphors, J. Lumin 219 (2020) 116917, https://doi.org/10.1016/j.jlumin.2019.116917.

[48] K. Van den Eeckhout, P.F. Smet, D. Poelman, Persistent luminescence in Eu2+-Doped compounds: a review, Materials 3 (2010) 2536–2566, https://doi.org/10.3390/ma3042536.

[49] W. Peng, H. Xia, Z. Zhang, T. Qi, S. Kong, W. Dai, Z. Huang, A surface corrosion and expansion mechanism on thermal degradation of $SrAl_2O_4$:Eu^{2+}, Dy^{3+}, J. Alloy. Compd. 753 (2018) 35–40, https://doi.org/10.1016/j.jallcom.2018.04.211.

[50] D. Yang, Q. Pan, S. Kang, G. Dong, J. Qiu, weakening thermal quenching to enhance luminescence of Er^{3+} doped β-$NaYF_4$ nanocrystals via acid-treatment, J. Am. Ceram. Soc. 102 (2019) 6027–6037, https://doi.org/10.1111/jace.16398.

[51] M. Quintanilla, N.O. Núñez, E. Cantelar, M. Ocaña, F. Cussó, Tuning from blue to magenta the up-converted emissions of YF_3:Tm^{3+}/Yb^{3+} nanocrystals, Nanoscale 3 (2011) 1046–1052, https://doi.org/10.1039/C0NR00676A.

[52] J. Liu, A.M. Kaczmarek, R. Van Deun, Concentration and temperature dependent upconversion luminescence of $CaWO_4$: Er^{3+},Yb^{3+} 3D microstructure materials, J. Lumin. 188 (2017) 604–611, https://doi.org/10.1016/j.jlumin.2017.05.022.

[53] Deutsche Norm, Phosphorescent pigments and products – part 1: measurement and marking at the producer, 11, DIN 67510 (2009) 2009, 11.

[54] A. Barbero-Castillo, F. Riefolo, C. Matera, S. Caldas-Martínez, P. Mateos-Aparicio, J.F. Weinert, A. Garrido-Charles, E. Claro, M.V. Sanchez-Vives, P. Gorostiza, Control of brain state transitions with a photoswitchable muscarinic agonist, Adv. Sci. 8 (2021) 2005027, https://doi.org/10.1002/advs.202005027.

[55] C. Matera, A.M.J. Gomila, N. Camarero, M. Libergoli, C. Soler, P. Gorostiza, Photoswitchable antimetabolite for targeted photoactivated chemotherapy, J. Am. Chem. Soc. 140 (2018) 15764–15773, https://doi.org/10.1021/jacs.8b08249.

[56] L. Camerin, G. Maleeva, A.M.J. Gomila, I. Suárez-Pereira, C. Matera, D. Prischich, E. Opar, F. Riefolo, E. Berrocoso, P. Gorostiza, Photoswitchable carbamazepine analogs for non-invasive neuroinhibition in vivo, Angew. Chem. Int. Ed. 63 (2024) e202403636, https://doi.org/10.1002/anie.202403636.

[57] J.M. Sanchez-Sanchez, F. Riefolo, A. Barbero-Castillo, R. Sortino, L. Agnetta, A. Manasanch, C. Matera, M. Bosch, M. Forcella, M. Decker, P. Gorostiza, M. V. Sanchez-Vives, Control of cortical slow oscillations and epileptiform discharges with photoswitchable type 1 muscarinic ligands, PNAS Nexus 4 (2025) pgaf009.